Structural and magnetic properties of antiferromagnetic Ce₂IrGa₁₂

Y. J. Zhang,[1] B. Shen [ORCID],[1] F. Du,[1] Y. Chen,[1] J. Y. Liu,[2] Hanoh Lee,[1,3,*] M. Smidman [ORCID],[1,†] and H. Q. Yuan[1,4]

[1]*Center for Correlated Matter and Department of Physics, Zhejiang University, Hangzhou 310058, China*
[2]*Department of Chemistry, Zhejiang University, Hangzhou 310027, China*
[3]*Center for Quantum Materials and Superconductivity, Department of Physics, SungKyunKwan University, Suwon 16419, Republic of Korea*
[4]*Collaborative Innovation Center of Advanced Microstructures, Nanjing University, Nanjing 210093, China*

We report on a study of the structural and magnetic properties of single crystals of Ce₂IrGa₁₂. Ce₂IrGa₁₂ crystallizes in a layered tetragonal structure and undergoes an antiferromagnetic transition below 3.1 K. We characterize the temperature-field phase diagrams of Ce₂IrGa₁₂ for fields both within the *ab* plane and along the *c* axis, where the presence of a field-induced magnetic phase is found for in-plane fields. The ordering temperature is moderately enhanced upon the application of pressures up to 2.3 GPa, suggesting that Ce₂IrGa₁₂ corresponds to the well-localized region of the Doniach phase diagram.

I. INTRODUCTION

Ce-based intermetallic compounds have attracted extensive interest owing to their exotic properties and fascinating underlying physics, such as complex magnetic order, unconventional superconductivity, and quantum criticality [1–3]. In these systems, the periodically arranged localized $4f$ moments are screened by the conduction electrons via the Kondo effect. Another competing interaction is the Ruderman-Kittel-Kasuya-Yosida interaction which favors long-range magnetic order [4–6], and the competition between these interactions gives rise to a variety of ground states [7], which may be tuned by pressure, magnetic fields, or chemical doping [1].

Ce_nMIn_{3n+2} ($M=$transition metal) systems show a variety of unusual phenomena, including the coexistence of magnetism and superconductivity, non-Fermi-liquid behavior near a magnetic instability, and multiple quantum phase transitions upon tuning with different parameters [8–10]. Ce_nMIn_{3n+2} are formed from MIn_2 and $CeIn_3$ layers, which are stacked along the c axis [11], where $CeIn_3$ itself exhibits antiferromagnetic order below $T_N = 10.1$ K at ambient pressure, as well as a pressure-induced superconducting dome with a maximum transition temperature of $T_c^{max} = 0.2$ K near a quantum critical point [12]. Among the $CeMIn_5$ series, $CeCoIn_5$ [13] and $CeIrIn_5$ [14] are unconventional superconductors at ambient pressure with $T_c = 2.3$ and 0.4 K, respectively, while $CeRhIn_5$ shows antiferromagnetic ordering below $T_N = 3.8$ K and pressure-induced superconductivity with T_c reaching 2.1 K at 2.1 GPa [15]. These findings gave a strong indication that increasing the quasi-two-dimensionality can significantly enhance T_c of heavy-fermion superconductors.

In comparison, the Ce_2MIn_8 compounds consist of two $CeIn_3$ layers separated by a layer of MIn_2, and therefore, the dimensionality is between that of $CeIn_3$ and $CeMIn_5$

[16]. Correspondingly, Ce_2CoIn_8 [17] and Ce_2PdIn_8 [18] are heavy-fermion superconductors at ambient pressure with intermediate T_c values of 0.4 and 0.68 K, respectively, while Ce_2RhIn_8 is a heavy-fermion antiferromagnet exhibiting pressure-induced superconductivity with a maximum T_c of 2 K near 2.3 GPa [19]. Interestingly, Ce_2PdIn_8 was found to exhibit nodal superconductivity together with a field-induced quantum critical point at the upper critical field [20], which is strikingly similar to the behavior observed in $CeCoIn_5$ [13,21]. Meanwhile, the crystal structures of Ce_3PtIn_{11} and Ce_3PdIn_{11} have two inequivalent Ce sites, and both compounds show the coexistence at ambient pressure of complex magnetic ground states with multiple magnetic transitions and heavy-fermion superconductivity with T_c of 0.3 and 0.4 K, respectively [22–25].

Efforts have been made to look for isostructural gallides in the Ce_nMGa_{3n+2} series with Ga instead of In. This is in particular due to the discovery that $PuCoGa_5$ is a superconductor with $T_c = 18.5$ K [26], which is the largest among the heavy-fermion superconductors and much higher than isostructural $PuCoIn_5$ [27,28]. Instead, however, a number of different structures are found to occur. $CeGa_6$ has a tetragonal structure (space group $P4/nbm$) and is an antiferromagnet with $T_N \sim 1.7$ K [29]. Ce_2MGa_{12} ($M =$ Cu, Ni, Pt, Pd, Rh) crystallizes in a layered tetragonal structure with the same space group, $P4/nbm$, in which layers of $CeGa_6$ are inserted between two layers of MGa_6. Ce_2PdGa_{12} is a strongly anisotropic antiferromagnet with $T_N = 11$ K, where a ferromagnetic in-plane component appears below a second transition at 5 K [30,31]. Ce_2NiGa_{12} and Ce_2RhGa_{12} are reported to order antiferromagnetically at 10 and 3.5 K, respectively [32,33], while Ce_2PtGa_{12} exhibits two antiferromagnetic transitions at $T_{N1} = 7.3$ K and $T_{N2} = 5.5$ K [34]. Upon applying pressure, T_N of Ce_2PdGa_{12} is suppressed, giving rise to a nonmagnetic state at a critical pressure of around $P_c \sim 7$ GPa [35]. Meanwhile, the antiferromagnetism of Ce_2NiGa_{12} disappears at $P_c \sim 5.5$ GPa, while the Ce valence drastically changes at a higher pressure of $P_V \sim 9$ GPa [36].

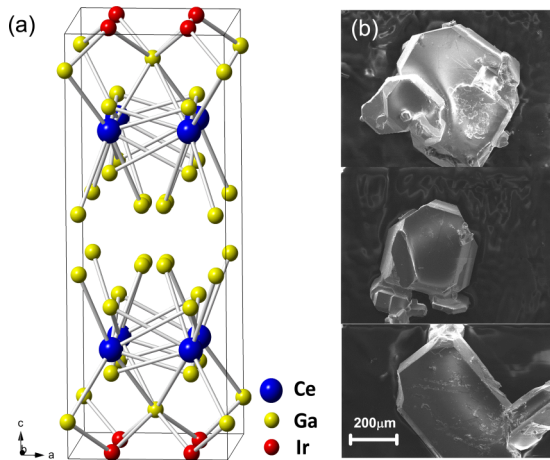*hlee.rtf@gmail.com
†msmidman@zju.edu.cn

FIG. 1. (a) Crystal structure of Ce_2IrGa_{12}, where blue, red, and yellow represent the Ce, Ir, and Ga atoms, respectively. (b) Scanning electron microscope image showing the morphology of the Ce_2IrGa_{12} single crystals.

Compared to the two aforementioned compounds, Ce_2RhGa_{12} has much lower T_N, and it is of particular interest to examine Ce_2MGa_{12} compounds with a lower T_N in order to determine whether they are situated in closer proximity to quantum criticality. Here we report the synthesis of single crystals of isostructural Ce_2IrGa_{12} using a flux method. The physical properties are investigated using electrical resistivity, magnetic susceptibility, and specific-heat measurements, and we find that Ce_2IrGa_{12} is an antiferromagnet below $T_N = 3.1$ K at ambient pressure. The temperature-field phase diagrams are constructed for $H||ab$ and $H||c$, where T_N is suppressed upon applying fields, and a metamagnetic transition is observed for fields applied within the ab plane. T_N shows a moderate enhancement upon applying pressures up to 2.3 GPa, indicating that Ce_2IrGa_{12} is situated on the well-localized side of the Doniach phase diagram.

II. EXPERIMENTAL DETAILS

Single crystals of Ce_2IrGa_{12} were grown using a flux method. Ce_2Ir was first prepared by arc melting Ce ingot (99.9%) and Ir powder (99.99%) in a titanium-gettered argon atmosphere. Ce_2Ir and Ga (99.99%) were then placed in an alumina crucible in a 1:40 atomic ratio and sealed in an evacuated quartz tube. The tube was heated up to 1150 °C and held at this temperature for 24 h, before being cooled slowly to 400 °C and centrifuged to remove excess Ga. Shiny cuboidlike samples, with typical lengths of 0.2–0.55 mm, were obtained, and the phase was determined to be Ce_2IrGa_{12} using single-crystal x-ray diffraction (XRD) and a cold field emission scanning electron microscope (SEM) equipped with an x-ray energy spectrometer. Images of the Ce_2IrGa_{12} crystals are shown in Fig. 1(b), which were obtained using the SEM. The single crystals of La_2IrGa_{12}, which were used as a nonmagnetic analog, were synthesized using an analogous method. Single-crystal XRD measurements were performed using an Xcalibur, Atlas, Gemini ultra diffractometer with an x-ray wavelength of $\lambda = 0.71073$ Å. The electrical resistivity, magnetic susceptibility, and heat capacity were all measured
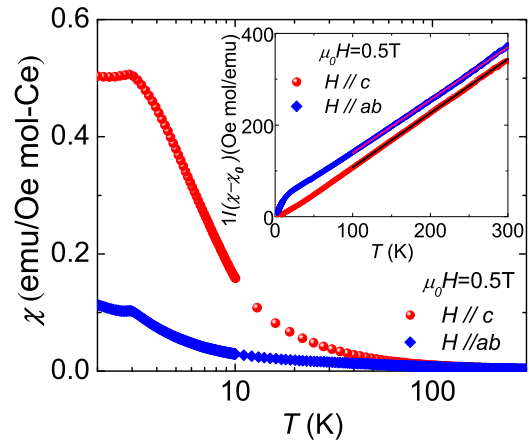

FIG. 2. Temperature dependence of the magnetic susceptibility $\chi(T)$ of Ce_2IrGa_{12} measured in an applied field of 0.5 T both parallel to the c axis and in the ab plane. The inset shows $1/(\chi - \chi_0)$ for the two field directions, and the lines show the Curie-Weiss fitting.

using a Physical Property Measurement System (PPMS-14 T), including a vibrating sample magnetometer option and a ^{3}He refrigerator insert. The electrical transport measurements under pressure were carried out in a piston-cylinder clamp-type cell. The resistivity measurements were performed with the current in the ab plane, with the field and current directions perpendicular.

III. RESULTS

A. Crystal structure

Single-crystal x-ray diffraction was performed to characterize the crystal structure. The results of the refinement of the data are displayed in Table I. They show that Ce_2IrGa_{12} crystallizes in the same tetragonal structure as other Ce_2MGa_{12} compounds with space group $P4/nbm$ [30,32,37], as displayed in Fig. 1(a). The refined lattice parameters are $a = 6.0614(4)$ Å and $c = 15.6818(13)$ Å, which are similar to those of Ce_2RhGa_{12} [37].

B. Antiferromagnetic transitions in Ce_2IrGa_{12}

Figure 2 displays the temperature dependence of the magnetic susceptibility $\chi(T)$ of Ce_2IrGa_{12} measured in an applied field of $\mu_0H = 0.5$ T both parallel to the c axis and within the ab plane. The low-temperature $\chi(T)$ for $H||c$ and $H||ab$ both exhibit a peak at T_N. The lack of hysteresis between zero-field-cooling and field-cooling measurements indicates that the transition is antiferromagnetic. The value of χ for $H||c$ is higher than for $H||ab$, indicating that the c axis is the easy axis of magnetization. For both field directions, the data for Ce_2IrGa_{12} follow Curie-Weiss behavior from 300 K down to around 100 K. The magnetic susceptibility for both orientations was fitted to a modified Curie-Weiss law: $\chi = \chi_0 + C/(T - \theta_P)$ from 100 to 300 K, where χ_0 is the temperature-independent term, C is the Curie constant, and θ_P is the Curie-Weiss temperature. The derived effective moments are $2.57\mu_B$/Ce ($H||c$) and $2.58\mu_B$/Ce ($H||ab$), with $\theta_P = 10.2(2)$ K ($H||c$) and $-22.6(5)$ K ($H||ab$). These values

TABLE I. Results from refining single-crystal XRD measurements of Ce_2IrGa_{12}, where the refinement parameters R_1, wR_2; atomic coordinates; and isotropic displacement parameters U_{eq} are displayed.

Parameter	Value			
Formula	Ce_2IrGa_{12}			
Space group	$P4/nbm$ (No. 125)			
Lattice parameters	$a = 6.0614(4)$ Å, $c = 15.6818(13)$ Å			
R_1, wR_2	0.0529, 0.1504			
Atom	x	y	z	U_{eq}
Ir1	0.75	0.25	0.00	0.0059(5)
Ce1	0.75	0.25	0.24261(9)	0.0063(5)
Ga1	0.5002(2)	0.4998(2)	0.08626(12)	0.0075(6)
Ga2	0.25	0.25	0.1864(2)	0.0078(7)
Ga3	0.25	0.25	0.34204(19)	0.0117(8)
Ga4	0.4304(3)	0.5696(3)	0.42914(14)	0.0211(7)

indicate an anisotropic θ_P, where the spins are antiferromagnetically coupled within the ab plane and ferromagnetically coupled along the c axis.

Figure 3 shows the temperature dependences of the magnetic specific heat C_{mag}/T and entropy S_{mag} of Ce_2IrGa_{12}, where C_{mag}/T was obtained by subtracting the lattice contribution, estimated from the data of nonmagnetic isostructural La_2IrGa_{12}. The total specific heats of Ce_2IrGa_{12} and La_2IrGa_{12} are displayed in the inset. A sharp jump in C_{mag}/T occurs at $T_N = 3.1$ K, which is typical of a second-order phase transition. The specific heat of La_2IrGa_{12} below 5 K was fitted using $C/T = \gamma + \beta T^2$, giving rise to a Sommerfeld coefficient $\gamma = 16.6(6)$ mJ/mol K^2 and $\beta = 2.84(4)$ mJ/mol K^4. A Debye temperature of $\theta_D = 217.4$ K was calculated using $\theta_D = \sqrt[3]{12\pi^4 nR/5\beta}$, where $n = 15$ is the number of atoms per formula unit and $R = 8.314$ J/mol K. The same expression was fitted to the data for Ce_2IrGa_{12} in the paramagnetic state between 10 and 20 K, giving rise to $\gamma = 144.4$ mJ/mol Ce K^2, $\beta = 2.86(8)$ mJ/mol K^4, and $\theta_D = 216.8$ K. A similarly large γ of 140 mJ/mol Ce K^2 was reported for Ce_2PdGa_{12}, obtained from data at $T > T_N$ [30], while larger values of

191 and 212 mJ/mol Ce K^2 were found for Ce_2NiGa_{12} and Ce_2RhGa_{12} [32,33]. However, we note that an enhanced γ deduced from data above T_N does not necessarily indicate heavy-fermion behavior with large effective carrier masses, but may arise due to the presence of magnetic correlations above T_N. The magnetic entropy S_{mag} of Ce_2IrGa_{12} was obtained by integrating C_{mag}/T of Ce_2IrGa_{12}. The magnetic entropy S_{mag} per Ce released at T_N is around half of $R \ln 2$ and reaches $R \ln 2$ at around 20 K. The enhanced C/T at low temperatures and reduced entropy at T_N may be due to the Kondo effect or a consequence of strongly anisotropic magnetic fluctuations above T_N.

The temperature dependences of the resistivity $\rho(T)$ of Ce_2IrGa_{12} and nonmagnetic isostructural La_2IrGa_{12} are shown in Fig. 4(a) down to 0.5 K, both of which show metallic behavior. The residual resistivity ρ_0 and residual resistivity ratio $[= \rho(300 \, K)/\rho(0.5 \, K)]$ are around 8.7 $\mu\Omega$ cm and 7.4, respectively, which are typical values for the samples synthesized. The magnetic contribution $\rho_{mag}(T)$ of Ce_2IrGa_{12}, obtained from subtracting the data for La_2IrGa_{12}, is displayed in Fig. 4(b). There is a broad maximum around $T^* = 51$ K in $\rho_{mag}(T)$ of Ce_2IrGa_{12}, which is typical of Kondo-lattice systems. As shown in the inset, upon further decreasing the temperature, there is an abrupt anomaly in $\rho(T)$, corresponding to the antiferromagnetic transition. $\rho(T)$ of Ce_2IrGa_{12} below T_N can be well described by [39]

$$\rho(T) = \rho_0 + AT^2 + b\Delta^2 \sqrt{\frac{T}{\Delta}} \exp\left(-\frac{\Delta}{T}\right)$$
$$\times \left[1 + \frac{2}{3}\frac{T}{\Delta} + \frac{2}{15}\left(\frac{T}{\Delta}\right)^2 \right], \tag{1}$$

where the second term corresponds to the Fermi-liquid contribution and the third term represents scattering by antiferromagnetic (AFM) spin-wave excitations with a spin-wave gap Δ. The fitted parameters for the data in zero field are $\rho_0 = 8.50(1) \, \mu\Omega$ cm, $A = 0.61(1) \, \mu\Omega$ cm K^{-2}, $b = 1.64(1) \, \mu\Omega$ cm K^{-2}, and $\Delta = 8.53(8)$ K. The sizable value of Δ relative to T_N, compared to Ce_2PdGa_{12}, which has $\Delta = 16$ K and $T_N = 10.5$ K [31], suggests the presence of a stronger magnetocrystalline anisotropy in Ce_2IrGa_{12}.
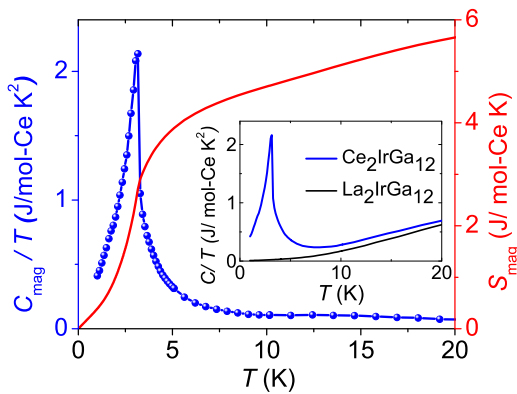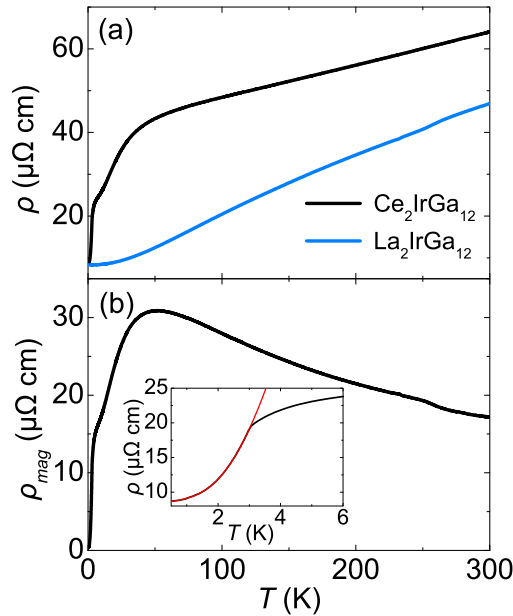

FIG. 3. Temperature dependence of the magnetic specific heat C_{mag}/T and magnetic entropy S_{mag} for Ce_2IrGa_{12}, where C_{mag}/T is obtained from subtracting an estimate of the lattice contribution from the La analog. In order to estimate S_{mag}, C_{mag}/T was extrapolated to zero temperature [38]. The inset displays the total specific heat as C/T of Ce_2IrGa_{12} (blue line) and La_2IrGa_{12} (black line).

FIG. 4. (a) Temperature dependence of the resistivity $\rho(T)$ of Ce_2IrGa_{12} and La_2IrGa_{12}. (b) Temperature dependence of the magnetic contribution to the resistivity $\rho_{mag}(T)$ of Ce_2IrGa_{12}, obtained from subtracting the lattice contribution. The inset shows the low-temperature $\rho(T)$ of Ce_2IrGa_{12}. The red solid line shows the results from fitting with Eq. (1).

C. Temperature-magnetic-field phase diagram

The temperature dependence of C/T for Ce_2IrGa_{12} is displayed in Fig. 5, measured with various magnetic fields applied along the c axis. The jump corresponding to T_N gradually shifts to lower temperature with increasing magnetic field for $\mu_0 H < 2.2$ T, as expected for an antiferromagnetic transition. For fields higher than 2.2 T, no transition is observed, but there is a broad maximum, which moves to higher temperatures with increasing field. This likely corresponds to a Schottky contribution arising from Zeeman splitting of the ground-state doublet. No divergence is observed in
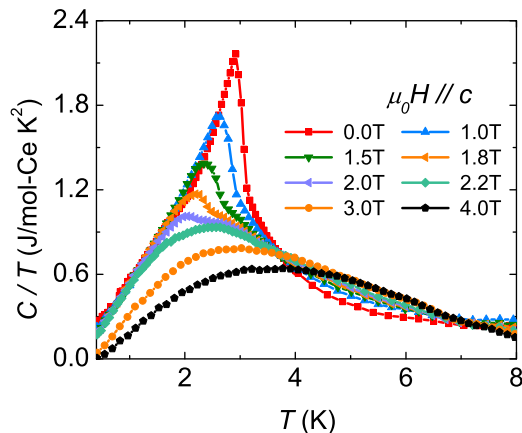

FIG. 5. Temperature dependence of C/T of Ce_2IrGa_{12}, which were measured in zero field and various fields applied along the c axis.
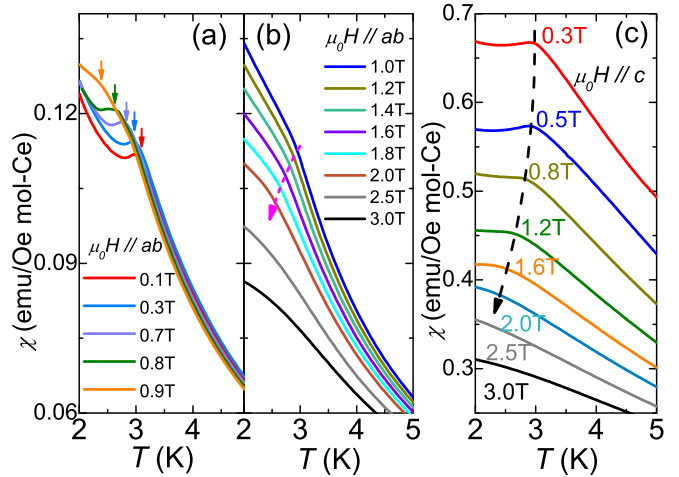

FIG. 6. (a) Temperature dependence of $\chi(T)$ measured with fields applied parallel to the ab plane below 0.9 T. The arrows mark the antiferromagnetic transition. (b) Temperature dependence of $\chi(T)$ measured with fields applied parallel to the ab plane beyond 0.9 T. The dashed arrow marks the position of the anomaly observed to develop at higher fields. (c) Temperature dependence of $\chi(T)$ measured with fields applied along the c axis. The dashed arrow marks the position of the antiferromagnetic transition with increasing field.

C/T upon suppressing the magnetism with applied magnetic field, indicating a lack of field-induced quantum criticality in Ce_2IrGa_{12}.

The temperature dependence of $\chi(T)$ in various fields for two orientations is displayed in Figs. 6(a) and 6(b) for $H\|ab$ and Fig. 6(c) for $H\|c$. In a field of 0.1 T, $\chi(T)$ shows a peak at 3.1 K for both $H\|ab$ and $H\|c$, corresponding to the antiferromagnetic transition. For $H\|ab$, the peak positions marked by the arrows in Fig. 6(a) are suppressed rapidly to lower temperatures with increasing magnetic field, disappearing above 0.9 T. Above 0.9 T, a weaker anomaly is observed to emerge at higher temperatures, as indicated by the dashed line in Fig. 6(b). Upon further increasing field, this feature broadens and gradually moves to lower temperatures and is difficult to detect above 2 T. Meanwhile, for $H\|c$, as shown in Fig. 6(c), a clear anomaly is observed at T_N, below which $\chi(T)$ is nearly temperature independent. This transition is suppressed with field and is not observed in a 2 T field.

$\rho(T)$ of Ce_2IrGa_{12} for various fields applied parallel to the ab plane and c axis are shown in Figs. 7(a) and 7(b), respectively, with the current in the ab plane. The corresponding derivatives $d\rho(T)/dT$ are displayed in Figs. 7(c) and 7(d). At low fields, an anomaly is observed in $\rho(T)$ corresponding to the antiferromagnetic transition, and there is a sharp asymmetric peak in $d\rho(T)/dT$. At higher fields, a clear anomaly is not observed in $\rho(T)$, and $d\rho(T)/dT$ instead exhibits a broad symmetric peak, indicating the lack of a magnetic transition. For $H\|ab$, the transition is suppressed by field, but for fields below 0.9 T, the suppression appears to be less rapid with field than that of the peak in $\chi(T)$ [Fig. 6(a)]. Meanwhile, the anomaly becomes less pronounced with increasing applied field and is difficult to detect beyond 1.4 T. For $H\|c$, T_N is also gradually suppressed to lower temperatures with increasing
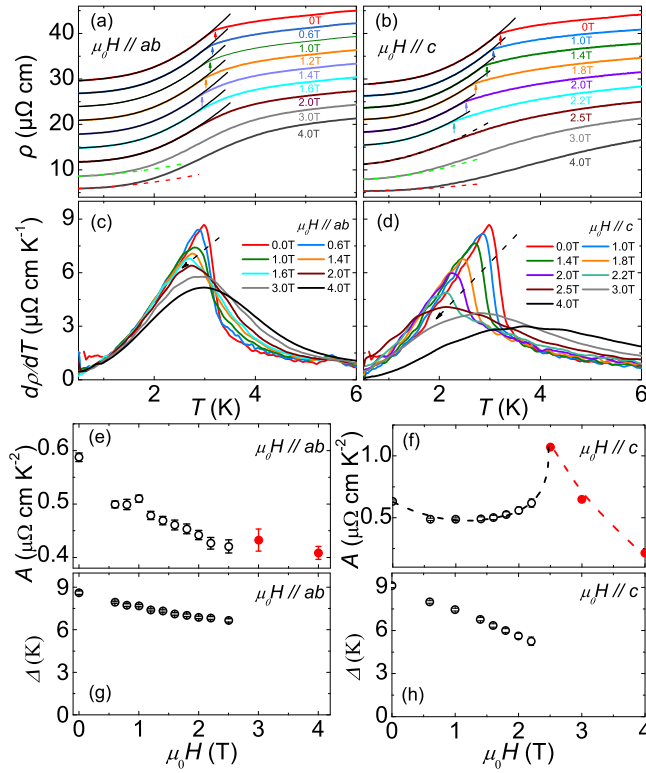
FIG. 7. $\rho(T)$ of Ce$_2$IrGa$_{12}$ in various fields applied parallel to the (a) ab plane and (b) c axis, with the current in the ab plane. The data are vertically shifted by $3\,\mu\Omega$ cm between adjacent fields, and the arrows correspond to the antiferromagnetic transition. The black solid lines show the results from fitting the data in the AFM state using Eq. (1), and the dashed lines correspond to fitting with Fermi-liquid behavior at higher fields. The derivatives $d\rho(T)/dT$ are displayed for fields parallel to the (c) ab plane and (d) c axis. The A coefficient is displayed as a function of applied field for (e) $H||ab$ and (f) $H||c$, derived from fitting the resistivity data. The black open symbols correspond to values obtained from fitting with Eq. (1) in the AFM state, while the red solid symbols are from fitting the data at higher fields using $\rho = \rho_0 + AT^2$. The field dependence of the spin wave gap Δ obtained from fitting using Eq. (1) is also displayed for (g) $H||ab$ and (h) $H||c$.

magnetic field, and the magnetic transitions are not observed at fields beyond 2.2 T. For both $H||ab$ and $H||c$, $\rho(T)$ follows Fermi-liquid behavior at higher fields, as shown by the dashed lines.

The in-field $\rho(T)$ data in the AFM state for both field directions were also analyzed using Eq. (1), and the field dependence of the A coefficient and Δ for $H||ab$ and $H||c$ are displayed in Figs. 7(e)–7(h). $\rho(T)$ were also analyzed at higher fields in the spin-polarized state using the Fermi-liquid expression $\rho(T) = \rho_0 + AT^2$. For $H||ab$, the A coefficient exhibits a drop upon the application of a field, which may be related to the emergence of the field-induced AF2 phase (see below). Upon further increasing the field, A continues to decrease, showing no enhancement at the transition to the spin-polarized phase. On the other hand, for $H||c$, the A coefficient shows an abrupt increase at the transition from the AFM to spin-polarized phase, reaching a maximum value at 2.5 T, before decreasing at higher fields. Such a
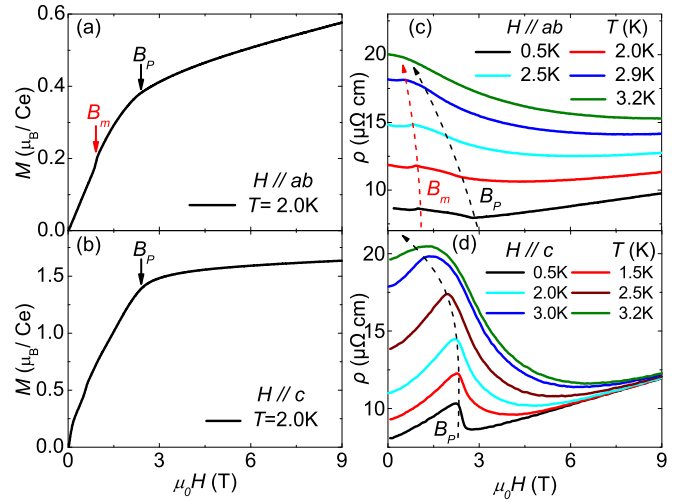

FIG. 8. Isothermal magnetization $M(H)$ of Ce$_2$IrGa$_{12}$ as a function of field at 2.0 K for (a) $H||ab$ and (b) $H||c$. Vertical arrows mark the metamagnetic transition B_m and the crossover B_p. The isothermal field dependence of the resistivity $\rho(H)$ of Ce$_2$IrGa$_{12}$ is displayed at various temperatures for fields applied parallel to the (c) ab plane and (d) c axis. The dashed lines mark the trend of B_m and B_p with temperature.

pronounced enhancement of the A coefficient at the field-induced metamagnetic transition to the spin-polarized phase is very similar to that observed in the heavy-fermion Ising antiferromagnet CeRh$_2$Si$_2$ for fields along the easy c axis [40,41]. Here this was ascribed to a significant enhancement of the effective mass, driven by the presence of critical magnetic fluctuations. Moreover, a similar enhancement is also observed in CeRh$_2$Si$_2$ at the pressure-induced suppression of antiferromagnetic order in the vicinity of the superconducting dome [42]. The field dependence of Δ for $H||ab$ and $H||c$ is displayed in Figs. 7(g) and 7(h). The magnetic field reduces Δ for both field directions, which is the expected behavior for antiferromagnetic systems [43].

Figures 8(a) and 8(b) display the isothermal magnetization $M(H)$ of Ce$_2$IrGa$_{12}$ at 2.0 K for fields in the ab plane and along the c axis. As displayed in Fig. 8(a), the magnetization for $H||ab$ at 2.0 K exhibits a kink at $B_m = 0.9$ T and a broad shoulder at $B_P = 2.5$ T. From a comparison of the $\chi(T)$ and $\rho(T)$ data, B_m likely corresponds to a metamagnetic transition from the low-field antiferromagnetic phase to a field-induced magnetic state, while the broad shoulder at $B_P = 2.5$ T may be the crossover from this field-induced phase to the spin-polarized state. In Fig. 8(b), the isothermal magnetization indicates that the c axis is the easy axis of magnetization, reaching $1.64\mu_B$/Ce for $H||c$ at 9 T and 2 K, compared to $0.58\mu_B$/Ce for $H||ab$. For $H||c$, the magnetization at 2 K shows only a broad crossover at 2.3 T, above which there is a much less rapid change with field, again suggesting a change to the spin-polarized state. There is a lack of hysteresis in both $M(H)$ and $\rho(H)$ upon increasing and decreasing the field, suggesting a second-order nature of the transitions.

The field-dependent resistivity $\rho(H)$ of Ce$_2$IrGa$_{12}$ at different temperatures is displayed in Fig. 8(c) for $H||ab$ and Fig. 8(d) for $H||c$. For $H||ab$, $\rho(H)$ at 0.5 K exhibits a
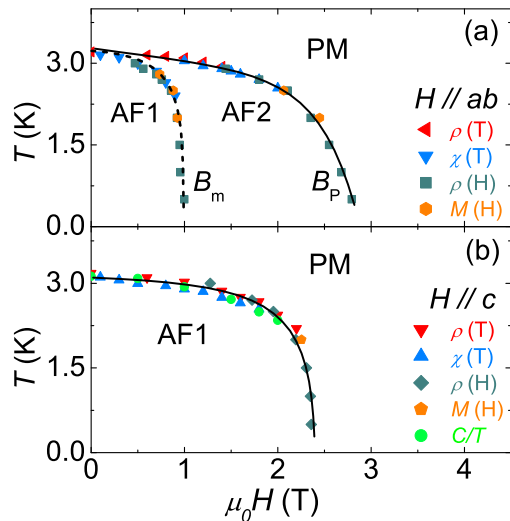
FIG. 9. The temperature-field phase diagram of Ce_2IrGa_{12} for magnetic fields applied (a) within the *ab* plane and (b) along the *c* axis, based on specific heat, resistivity, magnetoresistance, and magnetization measurements.
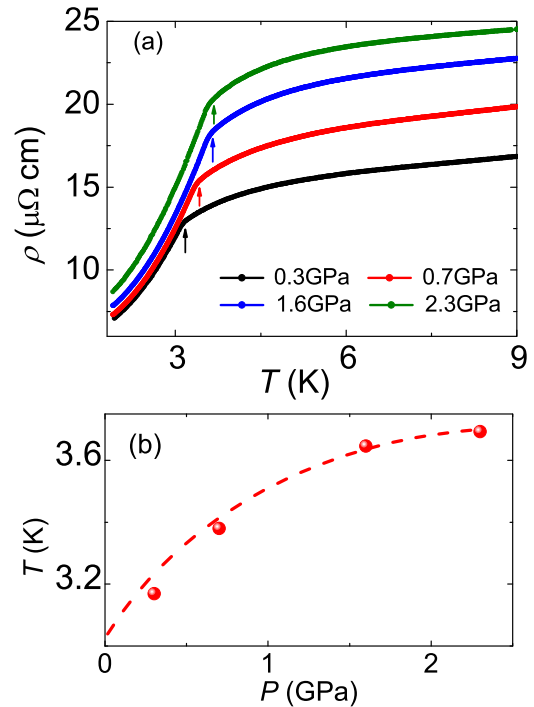

FIG. 10. (a) $\rho(T)$ of Ce_2IrGa_{12} under various pressures in zero applied field; the arrows correspond to the transition at T_N. (b) T-P phase diagram of Ce_2IrGa_{12}, where the symbols correspond to T_N and the dashed line is a guide to the eye.

peak at 1.0 T and a clear minimum with a sharp cusp at 2.8 T, which correspond to the metamagnetic transition at B_m and a crossover at B_P, respectively. Upon increasing the temperature, both B_m and B_P shift to lower fields, as indicated by the dashed lines, before disappearing above T_N. In the case of $H||c$, a broad hump is observed at 2.4 T at 0.5 K, which shifts to lower field with increasing temperature, indicating a crossover to the spin-polarized state.

Based on the measurements of resistivity, susceptibility, and specific heat of Ce_2IrGa_{12} with magnetic fields applied in the *ab* plane and along the *c* axis, we constructed the T-H phase diagrams, which are displayed in Fig. 9. For $H||ab$, the two boundaries of B_m and B_P are also shown in the phase diagram, and for in-plane fields there exists both a low-field antiferromagnetic phase (AF1) and a field-induced phase (AF2). B_m corresponds to the metamagnetic transition between the AF1 and AF2 phases, while B_P separates the AF2 and spin-polarized phases. For $H||c$, the phase boundaries obtained from $C(T)$, $\rho(T)$, $\rho(H)$, and $\chi(T)$ are all consistent, where T_N is continuously suppressed with field, before being no longer observed beyond 2.4 T.

D. Phase diagram in Ce_2IrGa_{12} under pressure

In order to examine the effects of hydrostatic pressure on the magnetic order and to look for pressure-induced quantum criticality in Ce_2IrGa_{12}, $\rho(T)$ was measured under various hydrostatic pressures up to 2.3 GPa, as displayed in Fig. 10(a). With increasing pressure, the magnitude of $\rho(T)$ above T_N increases, which may be due to enhanced Kondo scattering or magnetic scattering. T_N was determined from the onset of the resistivity anomaly, and the resulting phase diagram is displayed in Fig. 10(b). The T_N of Ce_2IrGa_{12} is found to be slightly enhanced upon applying pressure, to around 3.7 K at 2.3 GPa.

IV. DISCUSSION

Ce_2IrGa_{12} crystallizes in the tetragonal space group, $P4/nbm$ (No.125), in which the layers of $CeGa_6$ are inserted between two layers of $IrGa_6$, analogous to the structure of Ce_nMIn_{3n+2}. In Ce_2IrGa_{12}, the Ce-Ce interatomic distances are 3.031 Å in the *ab* plane and 8.073 Å along the *c* axis. This suggests the presence of anisotropic magnetic exchange interactions, which is supported by anisotropic Curie-Weiss temperatures of $\theta_P = -22.6$ K ($H||ab$) and 10.2 K ($H||c$). Anisotropic magnetic behaviors are also detected in other Ce_2MGa_{12} compounds, such as Ce_2RhGa_{12}, which also has an easy *c* axis and θ_P of -39 K for $H||ab$ and 5 K for $H||c$ [33].

The T_N values of Ce_2MGa_{12} for $M =$ Pd, Ni, Rh, and Ir are 11, 10, 3.5, and 3.1 K, respectively [30,32,33]. The unit cell volume of Ce_2IrGa_{12} (576.16 Å^3) is slightly larger than that of Ce_2NiGa_{12} (564.9 Å^3), while it is much smaller than that of Ce_2PdGa_{12} (579.64 Å^3) [30,32]. However, T_N of Ce_2IrGa_{12} is much lower than both the aforementioned compounds, suggesting that the substitution of different transition metals does not simply correspond to a chemical pressure effect but may otherwise tune the system, such as by modifying the electronic structure or carrier density. On the other hand, the substitution of Ir with Rh does correspond to a positive chemical pressure since the lattice volume of Ce_2RhGa_{12} is 573.1 Å^3, and T_N is enhanced slightly [33,37], which is consistent with our measurements of Ce_2IrGa_{12} under pressure. Furthermore, γ obtained from the C/T data above T_N is 212 mJ/mol Ce K^2 in Ce_2RhGa_{12} [33], which is larger than the value of 144.4 mJ/mol Ce K^2 we obtain for Ce_2IrGa_{12}.

T_N of Ce_2IrGa_{12} is enhanced to 3.7 K upon applying a pressure of 2.3 GPa. The moderate increase of T_N indicates that Ce_2IrGa_{12} is situated on the left side of the Doniach phase diagram, with weak coupling and well-localized $4f$ electrons [7]. Therefore, to look for quantum criticality in Ce_2IrGa_{12}, significantly larger pressures are likely necessary in order to sufficiently enhance the relative strength of the Kondo interaction. From Fig. 10(b), T_N at 2.3 GPa of 3.7 K appears to be close to the maximum value, which is very similar to T_N of Ce_2RhGa_{12}. On the other hand, Ce_2NiGa_{12} and Ce_2PdGa_{12} have considerably larger ordering temperatures, which are suppressed with pressure [35,36]. These results suggest that in the Ce_2MGa_{12} family, the systems with $M =$ Pd and Ni have larger energy scales for the magnetism than those with $M =$ Rh and Ir.

V. CONCLUSION

In summary, we have successfully synthesized single crystals of Ce_2IrGa_{12} using a flux method, which crystallizes in a layered tetragonal structure with space group $P4/nbm$ (No. 125). We found that Ce_2IrGa_{12} orders antiferromagnetically below $T_N = 3.1$ K. We constructed the temperature-field phase diagrams for both fields within the ab plane and along the c axis, where we found evidence for a metamagnetic transition to a different field-induced phase for in-plane fields. The reduced entropy at T_N and enhanced low-temperature C/T may be a consequence of the Kondo effect or short-range magnetic fluctuations, where the presence of the latter is also supported by a strongly anisotropic negative magnetoresistivity above T_N. Upon applying pressure, T_N undergoes a moderate enhancement for pressures up to 2.3 GPa. As a result, measurements at higher pressures are necessary to examine for the presence of quantum criticality, while neutron diffraction experiments could reveal the magnetic structure of both the zero-field and field-induced phases.

[1] Z. F. Weng, M. Smidman, L. Jiao, X. Lu, and H. Q. Yuan, Multiple quantum phase transitions and superconductivity in Ce-based heavy fermions, Rep. Prog. Phys. **79**, 094503 (2016).

[2] C. Pfleiderer, Superconducting phases of f-electron compounds, Rev. Mod. Phys. **81**, 1551 (2009).

[3] Q. Si and F. Steglich, Heavy fermions and quantum phase transitions, Science **329**, 1161 (2010).

[4] M. A. Ruderman and C. Kittel, Indirect exchange coupling of nuclear magnetic moments by conduction electrons, Phys. Rev. **96**, 99 (1954).

[5] T. Kasuya, A theory of metallic ferro- and antiferromagnetism on Zener's model, Prog. Theor. Phys. **16**, 45 (1956).

[6] K. Yosida, Magnetic properties of Cu-Mn alloys, Phys. Rev. **106**, 893 (1957).

[7] S. Doniach, The Kondo lattice and weak antiferromagnetism, Phys. B+C (Amsterdam) **91**, 231 (1977).

[8] J. S. Kim, J. Alwood, G. R. Stewart, J. L. Sarrao, and J. D. Thompson, Specific heat in high magnetic fields and non-Fermi-liquid behavior in $CeMIn_5(M = Ir, Co)$, Phys. Rev. B **64**, 134524 (2001).

[9] T. Park, F. Ronning, H. Q. Yuan, M. B. Salamon, R. Movshovich, and J. D. Thompson, Hidden magnetism and quantum criticality in the heavy fermion superconductor $CeRhIn_5$, Nature (London) **440**, 65 (2006).

[10] L. Jiao, Y. Chen, Y. Kohama, D. Graf, E. D. Bauer, J. Singleton, J. X. Zhu, Z. F. Weng, G. M. Pang, T. Shang, J. L. Zhang, H. O. Lee, T. Park, M. Jaime, J. D. Thompson, F. Steglich, Q. Si, and H. Q. Yuan, Fermi surface reconstruction and multiple quantum phase transitions in the antiferromagnet $CeRhIn_5$, Proc. Natl. Acad. Sci. USA **112**, 673 (2015).

[11] J. D. Thompson and Z. Fisk, Progress in heavy-fermion superconductivity: Ce115 and related materials, J. Phys. Soc. Jpn. **81**, 011002 (2012).

[12] G. Knebel, D. Braithwaite, P. C. Canfield, G. Lapertot, and J. Flouquet, The quantum critical point revisited in $CeIn_3$, High Pressure Res. **22**, 167 (2002).

[13] C. Petrovic, P. G. Pagliuso, M. F. Hundley, R. Movshovich, J. L. Sarrao, J. D. Thompson, Z. Fisk, and P. Monthoux, Heavy-fermion superconductivity in $CeCoIn_5$ at 2.3 K, J. Phys.: Condens. Matter **13**, L337 (2001).

[14] C. Petrovic, R. Movshovich, M. Jaime, P. G. Pagliuso, M. F. Hundley, J. L. Sarrao, Z. Fisk, and J. D. Thompson, A new heavy-fermion superconductor $CeIrIn_5$: A relative of the cuprates?, Europhys. Lett. **53**, 354 (2001).

[15] H. Hegger, C. Petrovic, E. G. Moshopoulou, M. F. Hundley, J. L. Sarrao, Z. Fisk, and J. D. Thompson, Pressure-Induced Superconductivity in Quasi-2D $CeRhIn_5$, Phys. Rev. Lett. **84**, 4986 (2000).

[16] A. L. Cornelius, P. G. Pagliuso, M. F. Hundley, and J. L. Sarrao, Field-induced magnetic transitions in the quasi-two-dimensional heavy-fermion antiferromagnets Ce_nRhIn_{3n+2} ($n = 1$ or 2), Phys. Rev. B **64**, 144411 (2001).

[17] G. Chen, S. Ohara, M. Hedo, Y. Uwatoko, K. Saito, M. Sorai, and I. Sakamoto, Observation of superconductivity in heavy-fermion compounds of Ce_2CoIn_8, J. Phys. Soc. Jpn. **71**, 2836 (2002).

[18] D. Kaczorowski, A. P. Pikul, D. Gnida, and V. H. Tran, Emergence of a Superconducting State from an Antiferromagnetic Phase in Single Crystals of the Heavy Fermion Compound Ce_2PdIn_8, Phys. Rev. Lett. **103**, 027003 (2009).

[19] M. Nicklas, V. A. Sidorov, H. A. Borges, P. G. Pagliuso, C. Petrovic, Z. Fisk, J. L. Sarrao, and J. D. Thompson, Magnetism and superconductivity in Ce_2RhIn_8, Phys. Rev. B **67**, 020506(R) (2003).

[20] J. K. Dong, H. Zhang, X. Qiu, B. Y. Pan, Y. F. Dai, T. Y. Guan, S. Y. Zhou, D. Gnida, D. Kaczorowski, and S. Y. Li, Field-Induced Quantum Critical Point and Nodal Superconductivity in the Heavy-Fermion Superconductor Ce_2PdIn_8, Phys. Rev. X **1**, 011010 (2011).

[21] J. Paglione, M. A. Tanatar, D. G. Hawthorn, E. Boaknin, R. W. Hill, F. Ronning, M. Sutherland, L. Taillefer, C. Petrovic, and P. C. Canfield, Field-Induced Quantum Critical Point in $CeCoIn_5$, Phys. Rev. Lett. **91**, 246405 (2003).

[22] J. Prokleška, M. Kratochvílová, K. Uhlířová, V. Sechovský, and J. Custers, Magnetism, superconductivity, and quantum criticality in the multisite cerium heavy-fermion compound Ce_3PtIn_{11}, Phys. Rev. B **92**, 161114(R) (2015).

[23] D. Das, D. Gnida, Ł. Bochenek, A. Rudenko, M. Daszkiewicz, and D. Kaczorowski, Magnetic field driven complex phase diagram of antiferromagnetic heavy-fermion superconductor Ce_3PtIn_{11}, Sci. Rep. **8**, 16703 (2018).

[24] M. Kratochvílová, J. Prokleška, K. Uhlířová, V. Tkáč, M. Dušek, V. Sechovský, and J. Custers, Coexistence of antiferromagnetism and superconductivity in heavy fermion cerium compound Ce_3PdIn_{11}, Sci. Rep. **5**, 15904 (2015).

[25] D. Das, D. Gnida, and D. Kaczorowski, Anisotropic magneto-transport and magnetic phase diagrams of the antiferromagnetic heavy-fermion superconductor Ce_3PdIn_{11}, Phys. Rev. B **99**, 054425 (2019).

[26] J. L. Sarrao, L. A. Morales, J. D. Thompson, B. L. Scott, G. R. Stewart, F. Wastin, J. Rebizant, P. Boulet, E. Colineau, and G. H. Lander, Plutonium-based superconductivity with a transition temperature above 18 K, Nature (London) **420**, 297 (2002).

[27] E. D. Bauer, M. M. Altarawneh, P. H. Tobash, K. Gofryk, O. E. Ayala-Valenzuela, J. N. Mitchell, R. D. McDonald, C. H. Mielke, F. Ronning, J.-C. Griveau, E. Colineau, R. Eloirdi, R. Caciuffo, B. L. Scott, O. Janka, S. M. Kauzlarich, and J. D. Thompson, Localized 5f electrons in superconducting $PuCoIn_5$: Consequences for superconductivity in $PuCoGa_5$, J. Phys.: Condens. Matter **24**, 052206 (2011).

[28] B. J. Ramshaw, A. Shekhter, R. D. McDonald, J. B. Betts, J. N. Mitchell, P. H. Tobash, C. H. Mielke, E. D. Bauer, and A. Migliori, Avoided valence transition in a plutonium superconductor, Proc. Natl. Acad. Sci. USA **112**, 3285 (2015).

[29] E. Lidström, R. Wäppling, O. Hartmann, M. Ekström, and G. M. Kalvius, A μSR and neutron scattering study of $REGa_6$, where RE = Ce, Nd, Gd and Tb, J. Phys.: Condens. Matter **8**, 6281 (1996).

[30] R. T. Macaluso, J. N. Millican, S. Nakatsuji, H. O. Lee, B. Carter, N. O. Moreno, Z. Fisk, and J. Y. Chan, A comparison of the structure and localized magnetism in Ce_2PdGa_{12} with the heavy fermion $CePdGa_6$, J. Solid State Chem. **178**, 3547 (2005).

[31] D. Gnida and D. Kaczorowski, Magnetism and weak electronic correlations in Ce_2PdGa_{12}, J. Phys.: Condens. Matter **25**, 145601 (2013).

[32] J. Y. Cho, J. N. Millican, C. Capan, D. A. Sokolov, M. Moldovan, A. B. Karki, D. P. Young, M. C. Aronson, and J. Y. Chan, Crystal growth, structure, and physical properties of Ln_2MGa_{12} (Ln = La, Ce; M = Ni, Cu), Chem. Mater. **20**, 6116 (2008).

[33] S. Nallamuthu, T. P. Rashid, V. Krishnakumar, C. Besnard, H. Hagemann, M. Reiffers, and R. Nagalakshmi, Anisotropic magnetic, transport and thermodynamic properties of novel tetragonal Ce_2RhGa_{12} compound, J. Alloys Compd. **604**, 379 (2014).

[34] O. Sichevych, C. Krellner, Y. Prots, Y. Grin, and F. Steglich, Physical properties and crystal chemistry of $Ce_2Ga_{12}Pt$, J. Phys.: Condens. Matter **24**, 256006 (2012).

[35] S. Ohara, T. Yamashita, T. Shiraishi, K. Matsubayashi, and Y. Uwatoko, Pressure effects on electrical resistivity of heavy-fermion antiferromagnet Ce_2PdGa_{12}, J. Phys.: Conf. Ser. **400**, 042048 (2012).

[36] N. Kawamura, R. Sasaki, K. Matsubayashi, N. Ishimatsu, M. Mizumaki, Y. Uwatoko, S. Ohara, and S. Watanabe, High pressure properties for electrical resistivity and Ce valence state of heavy-fermion antiferromagnet Ce_2NiGa_{12}, J. Phys.: Conf. Ser. **568**, 042015 (2014).

[37] R. Nagalakshmi, R. Kulkarni, S. K. Dhar, A. Thamizhavel, V. Krishnakumar, C. Besnard, H. Hagemann, and M. Reiffers, Crystal growth and structure determination of the novel tetragonal compound Ce_2RhGa_{12}, Chem. Met. Alloys **4**, 229 (2011).

[38] M. A. Continentino, S. N. deMedeiros, M. T. D. Orlando, M. B. Fontes, and E. M. Baggio-Saitovitch, Anisotropic quantum critical behavior in $CeCoGe_{3-x}Si_x$, Phys. Rev. B **64**, 012404 (2001).

[39] M. B. Fontes, J. C. Trochez, B. Giordanengo, S. L. Bud'ko, D. R. Sanchez, E. M. Baggio-Saitovitch, and M. A. Continentino, Electron-magnon interaction in RNiBC (R = Er, Ho, Dy, Tb, and Gd) series of compounds based on magnetoresistance measurements, Phys. Rev. B **60**, 6781 (1999).

[40] W. Knafo, D. Aoki, D. Vignolles, B. Vignolle, Y. Klein, C. Jaudet, A. Villaume, C. Proust, and J. Flouquet, High-field metamagnetism in the antiferromagnet $CeRh_2Si_2$, Phys. Rev. B **81**, 094403 (2010).

[41] W. Knafo, R. Settai, D. Braithwaite, S. Kurahashi, D. Aoki, and J. Flouquet, Three-dimensional critical phase diagram of the Ising antiferromagnet $CeRh_2Si_2$ under intense magnetic field and pressure, Phys. Rev. B **95**, 014411 (2017).

[42] S. Araki, M. Nakashima, R. Settai, T. C. Kobayashi, and Y. Onuki, Pressure-induced superconductivity in an antiferromagnet $CeRh_2Si_2$, J. Phys.: Condens. Matter **14**, L377 (2002).

[43] E. Jobiliong, J. S. Brooks, E. S. Choi, H. Lee, and Z. Fisk, Magnetization and electrical-transport investigation of the dense Kondo system $CeAgSb_2$, Phys. Rev. B **72**, 104428 (2005).